





Accurate muonic interactions in neutron-star mergers and impact on heavy-element nucleosynthesis

Harry Ho-Yin Ng ¹, Carlo Musolino ¹, Samuel D. Tootle ² and Luciano Rezzolla ^{1,3,4}

¹*Institut für Theoretische Physik, Goethe Universität, Max-von-Laue-Str. 1, 60438 Frankfurt am Main, Germany*

²*Department of Physics, University of Idaho, Moscow, ID 83844, USA*

³*School of Mathematics, Trinity College, Dublin 2, Ireland*

⁴*Frankfurt Institute for Advanced Studies, Ruth-Moufang-Str. 1, 60438 Frankfurt am Main, Germany*

(Dated: December 2, 2024)

The abundances resulting from r -process nucleosynthesis as predicted by simulations of binary neutron-star (BNS) mergers remain an open question as the current state-of-the-art is still restricted to three-species neutrino transport. We present the first BNS merger simulations employing a moment-based general-relativistic neutrino transport with five neutrino species, thus including (anti)muons and advanced muonic β -processes, and contrast them with traditional three neutrino-species simulations. Our results show that a muonic trapped-neutrino equilibrium is established, forming a different trapped-neutrino hierarchy akin to the electronic equilibrium. The formation of (anti)muons and the muonization via muonic β -processes enhance the neutrino luminosity, leading to rapid cooling in the early post-merger phase. Since muonic processes redirect part of the energy otherwise used for protonization by electronic processes, they yield a cooler remnant and disk, together with neutrino-driven winds that are more neutron-rich. Importantly, the unbound ejected mass is smaller than three-species simulations and, because of its comparatively smaller temperature and proton fraction, it can enhance lanthanide production and reduce the overproduction of light r -process elements for softer equations of state. This finding underlines the importance of muonic interactions and five neutrino species in long-lived BNS remnants.

Introduction. The ejection of matter from binary neutron-star (BNS) mergers has long since been considered as one of the best sources for the synthesis of heavy elements via the r -process (see [1–4] for some reviews). The amount of this ejecta produced by a number of different mechanisms (e.g., shocks, neutrino-driven or magnetically driven winds, etc.) has been predicted by numerical simulations (see, e.g., [5–23]) and has found support in the recent observations of the GW170817 event (see, e.g., [24, 25]).

The kilonova signal associated with AT2017gfo displayed both “blue” and “red” components, attributed to lanthanide-poor, low-opacity ejecta (with electron fraction $Y_e \gtrsim 0.25$) and lanthanide-rich, high-opacity ejecta (with $Y_e \lesssim 0.25$), respectively [26–28]. Common explanations for the neutron-rich ejecta in BNS mergers include tidal disruption in asymmetric binaries and disk winds from prompt black hole collapse or short-lived hypermassive neutron star remnants [23, 29, 30]. However, recent studies suggest that a short-lived remnant alone cannot account for the kilonova brightness and duration [31]. Accurate modeling of the ejecta composition, light-curve, and lifetime of the remnant remains challenging given the difficulties of carrying-out long-term simulations [32, 33], but, more importantly, due to the uncertainties in the radiation transport and weak interactions [34–37]. Indeed, neutrino interactions significantly impact both ejecta composition and the formation of short gamma-ray bursts [38–40], as well as the post-merger dynamics [37, 41].

To date, most numerical simulations of BNS mergers assume the neutron stars to be made of neutrons (n), protons (p), electrons (e^-), and positrons (e^+), i.e., npe -matter. In this way, they neglect the presence of muons (μ^-), antimuons (μ^+), and obviously of muonic weak interactions due to their high rest-mass ($m_\mu = 105.7$ MeV). While this is a choice dictated by simplicity, core-collapse supernova simulations suggest that temperatures exceeding ~ 30 MeV can yield sub-

stantial muon production via electromagnetic and weak interactions [42]. Recent studies in simplified scenarios have started to explore the role of muonic interactions in BNS mergers, either using post-processed muonic interactions [43] or with $npe\mu$ -matter but an approximate (i.e., leakage-based) neutrino treatment [44]. In this Letter, we present the first comprehensive analysis of BNS mergers in full general relativity with $npe\mu$ -matter and employing a moment-based treatment of neutrino transport with five neutrino species.

Neutrino microphysics. As detailed in the End-Matter (EM), we have extended our three-species energy-integrated, moment-based M1 scheme `FIL-M1` [45] to evolve five neutrino species, with the addition of ν_μ and $\bar{\nu}_\mu$ and where tau neutrinos and antineutrinos (ν_τ and $\bar{\nu}_\tau$) are evolved as an effective species ν_x . Importantly, we have replaced the conventional opacities by the advanced ones provided by the state-of-the-art neutrino microphysical library `WeakHub` [46–48]. In particular, we have included the interactions listed in Table I in EM. All reaction rates, apart from pair processes (e), (f), and (g), are computed considering an energy dependence using 18 neutrino energy bins logarithmically spaced in the range [0.5, 420] MeV and tabulated after averaging in energy following Eqs. (A22)–(A27) in [36]. At runtime, the opacities interpolated from the table and emissivities are re-computed according to Kirchhoff’s law with the rescaled degeneracy parameters of the neutrinos. For pair processes, which are relevant only for heavy lepton-neutrinos, i.e., $\nu_{\mu,\tau}$ and $\bar{\nu}_{\mu,\tau}$, we calculate isotropic emissivities on-the-fly following Ref. [49] and apply Kirchhoff’s law for the corresponding absorption opacities (more details are presented in EM).

In addition to standard neutrino interactions for npe -matter, we also include muonic β -processes, but exclude inelastic muonic interactions (e.g., lepton flavor exchange between $\mu^-/+$ and $e^-/+$) since our approach is energy integrated (grey approximation) and we lack neutrino energy informa-

tion. On the other hand, the corresponding phase space-integrated opacities are significantly lower than the standard β -processes and elastic scattering at high densities [50–52]. Furthermore, due to the large rest-mass of μ^- , the use of an elastic approximation for muonic β -processes [44, 45, 53], can lead to significant discrepancies in the absorption opacity [48, 51]. To counter this, we employ full kinematics to account for momentum transfer, self-consistently incorporating weak magnetism, nuclear-form factors, pseudo-scalar effects, and medium modifications in the nucleon propagator for dense matter hadronic currents [48, 51, 52] (see EM for details).

To establish the impact of muonic interactions on neutron-star mergers remnants we simulated four equal-mass and irrotational BNSs with a total mass of $2.5 M_\odot$ and zero magnetic field to clearly isolate pure muonic effects from the complex MHD dynamics. To assess the robustness of the results, we employ two different realistic and temperature-dependent EOSs, SFHo [54] and DD2 [55], and for each EOS we consider scenarios with $npe\mu$ -matter (i.e., five neutrino species and denoted as $5-\nu$ hereafter) or with npe -matter (i.e., three neutrino species, or $3-\nu$). To compute the initial conditions with the FUKA solver [56, 57], we impose zero-temperature, neutrino-less weak equilibrium [44, 58] and, to avoid double-counting of electron contributions, we first subtract these from the table, then add different lepton contributions according to whether we are considering $npe\mu$ or npe matter. The grid extent for each simulation spans $[-1500 \text{ km}, 1500 \text{ km}]^3$ with seven refinement levels, and a finest grid spacing of $\Delta x \approx 280 \text{ m}$ [40, 59, 60]. Finally, as useful diagnostic quantities we introduce the out-of-weak-equilibrium chemical potentials $\mu_\Delta^{npl} := \mu_n - \mu_p - \mu_l$ (neutrinoless matter) and $\mu_\Delta^{npl\nu} := \mu_n - \mu_p - \mu_l - \mu_{\bar{\nu}_l}$ (neutrino-trapped matter), where μ_i represents the chemical potential (including rest-mass) for species n , p , and leptons $l = e, \mu$, and where μ_{ν_l} is computed from the neutrino fraction Y_{ν_l} [61].

Results. For compactness, the results presented hereafter will refer to the SFHo EOS, but corresponding (and similar) results for the DD2 EOS can be found in the Supplemental Material (SM). The top part of Fig. 1 illustrates the evolution of the maximum values of the rest-mass density ρ_{max} (blue lines), temperature T_{max} (red lines), and the temperature averages on the (x, y) -plane $\langle T \rangle_{xy}$ (red lines), for the $5-\nu$ (solid lines) and the $3-\nu$ scenarios (dashed lines). The data is shown as a function of the retarded time $\bar{t} := t - t_{\text{mer}}$, where $t_{\text{mer}} \simeq 18.8 \text{ ms}$ is the merger time [62], and differs by 0.5% in the two scenarios. Note that the $5-\nu$ scenario exhibits a stronger cooling driven by several processes: larger neutrino emission due to additional muonic processes, the generation of trapped neutrinos via the conversion of matter internal energy into radiation internal energy [35, 63], the creation of $\mu^- - \mu^+$ pairs from heating and the so-called “muonization”, i.e., the process where more $\bar{\nu}_\mu$ are emitted than ν_μ , thus building up a net muon-lepton number [42]. Muonization takes place mostly in the shocked, dense, high-temperature and sheared layers, increasing the muonic fraction Y_μ to $\sim 0.04 - -0.05$.

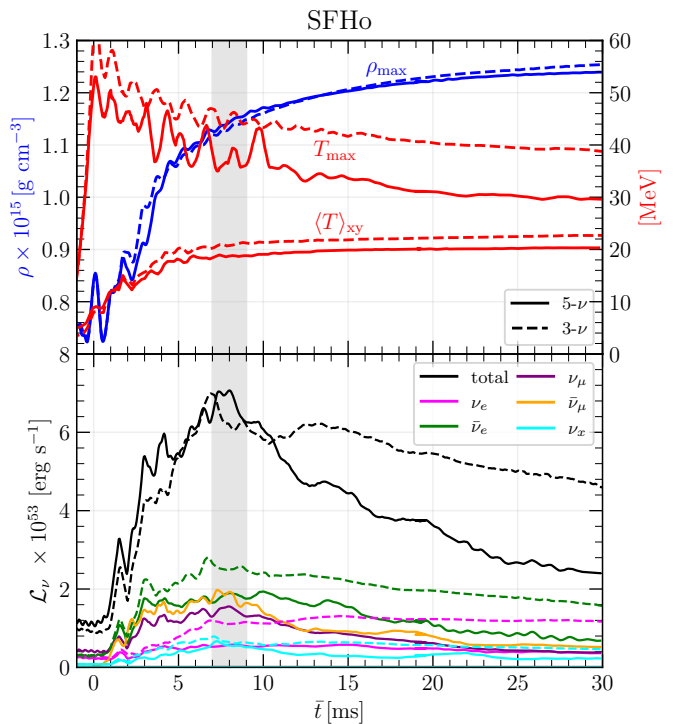


FIG. 1. *Top panel:* evolution of the maximum rest-mass density ρ_{max} , maximum temperature T_{max} , and mass-averaged temperature $\langle T \rangle_{xy}$ on the (x, y) -plane for the $5-\nu$ (solid lines) and $3-\nu$ scenarios (dashed lines). *Bottom panel:* neutrino luminosities (total and species specific) \mathcal{L}_ν at 300 km; the data is smoothed using a time-averaging over 0.2 ms. In both panels, the shaded region denotes the time when $\mu_\Delta^{npe\nu} \approx \mu_\Delta^{npp\nu} \approx 0$ (see Fig. 1 in SM).

However, it is considerably reduced as the matter moves outwards, where it reaches lower densities, lower temperatures, and “electronization” occurs more efficiently. The oscillatory behavior in T_{max} follows from alternating muonization and de-muonization in the hot spots of the two stellar cores, which significantly alters the temperature by converting or releasing electron degeneracy energy to form or absorb μ^- and μ^+ via muonic β -processes.

The bottom part of Fig. 1 shows both the total and the specific neutrino luminosities \mathcal{L}_ν across all species. In the $5-\nu$ scenario, both neutron stars start with a central $Y_\mu \approx 0.022$ and lower Y_e compared to the $3-\nu$ case [43]. The effects of the rapid muonization can be deduced from the fact that during the first 8 ms $\mathcal{L}_{\bar{\nu}_\mu}$ is $\sim 30\%$ larger than \mathcal{L}_{ν_μ} implying an excess of μ^- over μ^+ in the remnant. The emission of $\bar{\nu}_\mu$ (ν_μ) via μ^+ (μ^-) capture processes is able to extract a substantial amount of energy from the remnant as μ^+ capture processes tap energy that would otherwise be used in e^+ capture. This obviously favors $\mathcal{L}_{\bar{\nu}_\mu}$ over $\mathcal{L}_{\bar{\nu}_e}$ in $npe\mu$ -matter. Similarly, μ^- capture processes remove energy that would be used for e^- capture, thus resulting in an $\sim 12\%$ increase in the total emitted neutrino energy within the first 8 ms post-merger. The rapid increase in neutrino luminosity ends at

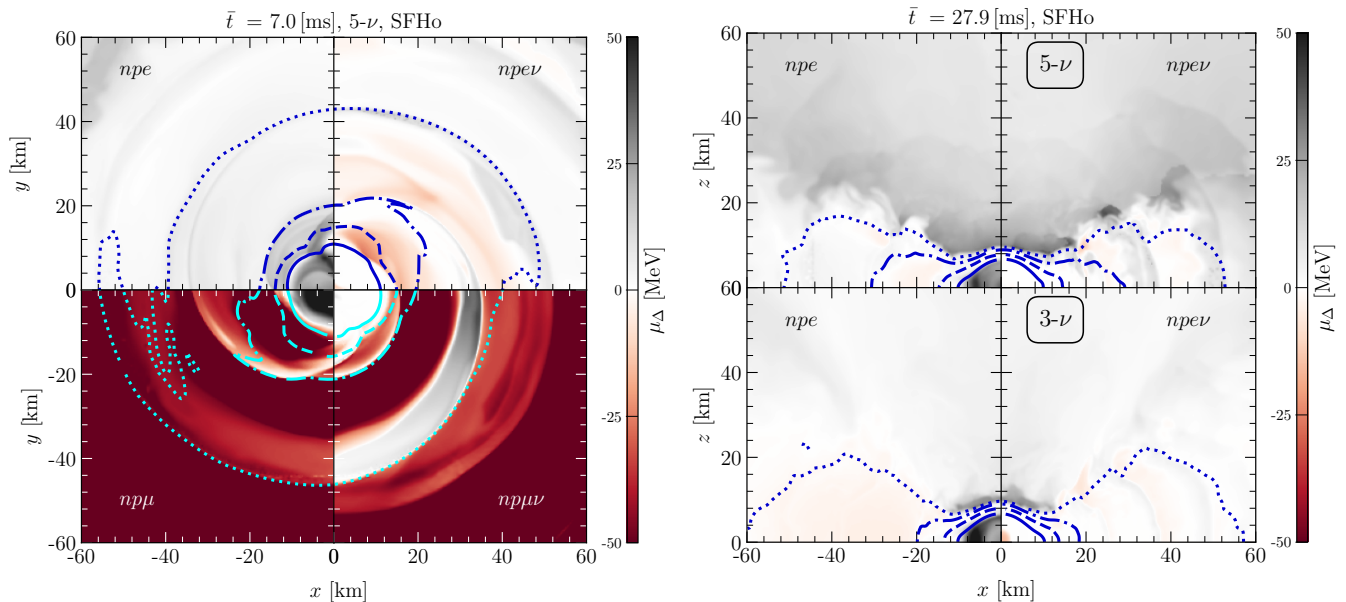


FIG. 2. *Left panel:* Equatorial distributions of the out-of-equilibrium chemical potentials μ_{Δ}^{npl} (left portions) and $\mu_{\Delta}^{npl\nu}$ (right portions) for lepton flavors $l = e, \mu$ in the 5- ν scenario at $\bar{t} = 7.0$ ms, i.e., when $\langle \mu_{\Delta}^{npl\nu} \rangle_{xy} \simeq 0$. The dotted, dash-dotted, dashed, and solid lines show rest-mass density contours at 10^{11} , 10^{12} , 10^{13} , and 10^{14} g cm^{-3} , respectively. *Right panel:* the same as in the left, but at $\bar{t} = 27.9$ ms and on the (x, z) -plane. For compactness, we show distributions for npe (left portions) and $npe\nu$ equilibria (right portions), but contrast the 5- ν (upper part) with the 3- ν scenario (bottom part). Note the considerable differences in the highest-density regions of the remnant.

$\bar{t} \approx 8$ ms, after which it declines rapidly. The start of this decline, which is marked with a grey-shaded area, corresponds to when the high-density matter reaches a muonic trapped-neutrino weak equilibrium (or $np\mu\nu$ -equilibrium) and is characterized by having $\langle \mu_{\Delta}^{np\mu\nu} \rangle_{xy} \approx 0$ (see Fig. 1 in SM), so that $\mathcal{L}_{\nu\mu}$ and $\mathcal{L}_{\bar{\nu}\mu}$ are significantly reduced. As to be expected, when this equilibrium starts to be reached around $\bar{t} \sim 9$ ms, the oscillations in T_{max} disappear.

The behavior described above is robust across the EOSs simulated here (see Fig. 1 in SM) and resembles the results reported in [44], where the late-time three-species total luminosity is smaller than in the five-species scenario, possibly because of the simpler leakage approach.

The rapid neutrino release in the early post-merger stages and the more efficient cooling – via neutrino emission, the generation of trapped neutrinos, $\mu^{-}\mu^{+}$ pairs, and via muonization – observed in the 5- ν scenario obviously leads to a colder remnant and hence to a significant reduction in ν -emission across all species, resulting in a $\sim 50\%$ lower total \mathcal{L}_{ν} at $\bar{t} = 30$ ms. This is somewhat in contrast to the findings in [44], where the adopted neutrino-leakage scheme cannot model trapped neutrinos and where luminosities do not strictly enforce energy conservation, leading to weaker cooling and overestimated neutrino luminosities that are not quite in agreement with the expected energy budget (see also [35]).

The process of $npl\nu$ -equilibration can be appreciated also from the left panel of Fig. 2, which reports distributions of μ_{Δ}^{npl} (left portions) and $\mu_{\Delta}^{npl\nu}$ (right portions) at $\bar{t} = 7.0$ ms for lepton flavors $l = e, \mu$ in the 5- ν scenario. Note that system

reaches $np\mu\nu$ and $npe\nu$ equilibria (i.e., $\mu_{\Delta}^{npl\nu} \simeq 0$) in regions with $\rho > 10^{14}$ g cm^{-3} , where significant neutrino trapping (due to elastic scattering and absorption processes) drives the system to recover the broken npe and $np\mu$ equilibria. These results, which are in qualitative agreement with previous simplified studies [61], indicate that the addition of new degrees of freedom and muonic weak interactions still leads to weak equilibria a few milliseconds after merger. The left panel of Fig. 2 also shows that $\mu_{\Delta}^{np\mu}$ exceeds μ_{Δ}^{npe} , indicating that substantially more $\bar{\nu}_{\mu}$ are trapped compared to $\bar{\nu}_{e}$. Additionally, the presence of non-zero Y_{μ} reduces μ_{e} [42], while μ^{+} capture partially replaces e^{+} capture; hence in the 5- ν scenario, $\mu_{\bar{\nu}_{e}}$ is decreased by $\sim 20 - 30$ MeV (see right panel of Fig. 2). Importantly, this phenomenology suggests that the neutrino trapping hierarchy normally encountered in simulations with three neutrino species, i.e., $\mu_{\bar{\nu}_{e}} > \mu_{\nu_{x}} > \mu_{\nu_{e}}$ [35], should be replaced by the new hierarchy $\mu_{\bar{\nu}_{\mu}} > \mu_{\bar{\nu}_{e}} > \mu_{\nu_{x}} > \mu_{\nu_{e}} > \mu_{\nu_{\mu}}$.

Special attention has been paid to assess how the inclusion of five neutrino species changes the composition of the remnant matter and the properties of the unbound ejecta, where we consider “unbound” matter satisfying the Bernoulli criterion $-hu_t > 1$ (here, h is the specific enthalpy and u_t the time component of the covariant fluid four-velocity) [64]. We recall that the ejection of matter from BNS mergers falls into two main classes depending on the associated timescale [17, 35, 65, 66]. More specifically, “dynamical” ejecta refers to matter that is lost over a timescale of tens of milliseconds around the merger as a result of tides, strong shocks, and large-amplitude oscillations. Conversely, “secular” refers to those ejecta pro-

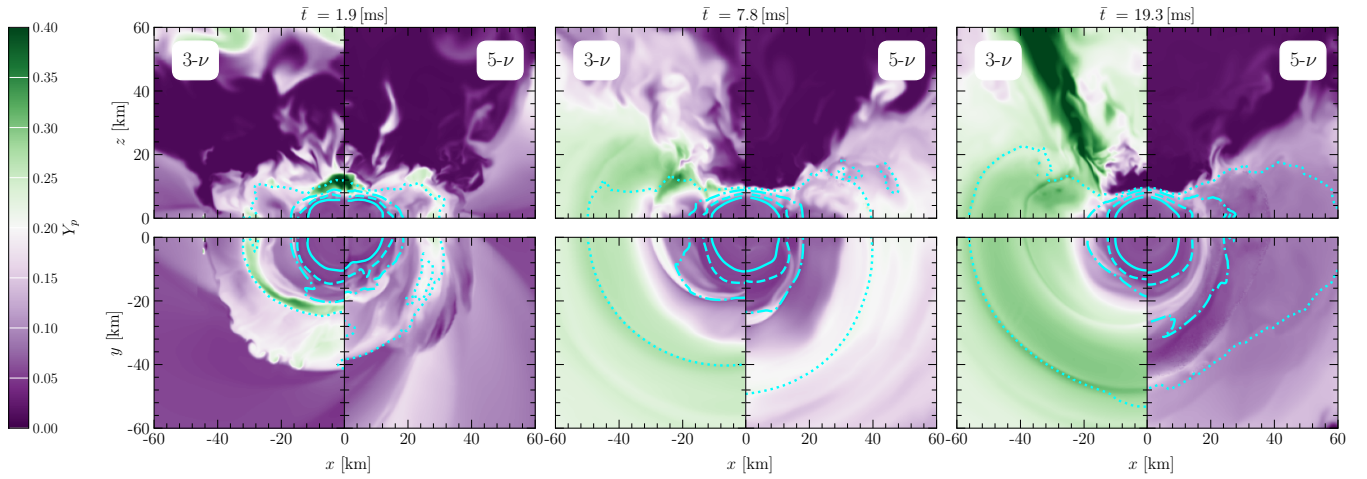


FIG. 3. Distributions of the proton fraction Y_p at $\bar{t} = 1.9$ ms (left column), 7.8 ms (middle column), and 19.3 ms (right column). The top (bottom) row shows the polar (equatorial) distributions and for each panel the left (right) portions refer to the 5- ν (3- ν) scenarios, respectively. Note the differences that develop and the significantly lower protonization at late times when accounting for five neutrino species.

duced over hundreds of milliseconds and that are the result of neutrino- or magnetically-driven winds (see e.g., [30] for a review)

Figure 3 is meant to illustrate the changes in the composition at three different times ($\bar{t} \simeq 2, 8,$ and 20 ms), either in the polar plane (top row) or in the equatorial one (bottom row), and both for the 3- ν (left part of each column) and for the 5- ν scenarios (right part). Soon after merger (left column), the protonization is weaker in the 5- ν scenario, as energy is redirected towards the creation of μ^- and μ^+ and muonic processes (muonization indirectly converts Y_e to Y_μ , thus reducing μ_e [42]). The net changes in $Y_p := Y_e + Y_\mu$ are due to differences in the rates of antilepton/lepton capture and, although the differences in $\mathcal{L}_{\bar{\nu}_\mu}$ and \mathcal{L}_{ν_μ} are small, these rates deprive the system of a significant amount of energy that would be spent in emitting $\bar{\nu}_e$ and ν_e , thereby reducing the gap between $\mathcal{L}_{\bar{\nu}_e}$ and \mathcal{L}_{ν_e} and inducing a weaker electronization. Furthermore, de-muonization occurs quickly in the ejecta, reducing Y_μ to $\lesssim 10^{-3}$ and resulting in dynamical ejecta that are less proton-rich, with $Y_p \approx Y_e$; this will have important nucleosynthetic consequences (see below).

These trends in neutrino luminosities persist throughout the simulation and become more pronounced at later times, as ν_e and $\bar{\nu}_e$ emissions are significantly suppressed, not only due to the colder remnant, but also because of the additional energy cost associated with muonic processes. This is supported by the observation that, despite the lower remnant temperature, for $\bar{t} \lesssim 12$ ms the combined heavy-lepton neutrino luminosity is larger in the 5- ν scenario, i.e., $\mathcal{L}_{\nu_\mu} + \mathcal{L}_{\bar{\nu}_\mu} + 2\mathcal{L}_{\nu_x}|_{5-\nu} > 4\mathcal{L}_{\nu_x}|_{3-\nu}$, where the luminosities on either side of the inequality refer to the five or three neutrino species, respectively. Moreover, the disk (i.e., the portion of the remnant with $\rho \lesssim 10^{12}$ g cm $^{-3}$) is cooler in the 5- ν case, which leads to a lower absorption opacity for ν_e and a weaker ν_e reabsorption. Additionally, the different hierarchy of trapped neutrinos

reduces $\mu_{\bar{\nu}_e}$ in a shell-like region of high temperature [67], resulting in reduced $\eta_{\bar{\nu}_e}$. This weakens the e^+ capture to produce p and $\bar{\nu}_e$ in the polar region. These factors significantly weaken protonization in the disk and polar regions as shown in the middle and right columns of Fig. 3 (right portions). By contrast, the 3- ν scenario features stronger electronization in the hotter disk that is driven by a stronger ν_e reabsorption and e^+ capture (left portions). Finally, since $\mu_\Delta^{np\mu} \lesssim -50$ MeV in regions with $\rho \lesssim 10^{14}$ g cm $^{-3}$ (see Fig. 2), μ^- are unlikely to survive in the comparatively low-density, low-temperature regions, thus leading to stronger (weaker) μ^- (μ^+) capture, i.e., to a net de-muonization ($Y_\mu/Y_p \sim 10^{-4} - 10^{-2}$) in the disk and at high-latitudes. Overall, our simulations reveal that a competition between muonic β -processes and electronic β -processes further weakens the protonization and leads to a more neutron-rich disk and high-latitude wind in the 5- ν scenario. However, because $\mu_\Delta^{np\mu} > 0$ in the disk and in high-latitude regions (see right panel of Fig. 2), gradual electronization is still occurring, albeit at a significantly slower rate than in a 3- ν scenario.

As a concluding aspect of our analysis, we study the composition of the unbound ejecta, collecting it on a 2-sphere with coordinate radius $r_{\text{ext}} = 300$ km, so that over a timescale of $\bar{t} = 28$ ms we measure a total amount $\approx 1.63 \times 10^{-3} M_\odot$ ($\approx 3.64 \times 10^{-3} M_\odot$) for the 5- ν (3- ν) scenario, respectively. The factor-two difference in the ejected matter in the 5- ν simulations is due to the combination of a larger initial neutrino luminosity – that deprives the system of kinetic energy – and of a consequent cooler remnant – that launches weaker neutrino-driven winds. Furthermore, while we measure a negligible fraction of muons ($Y_\mu \lesssim 5 \times 10^{-3}$), ejecta with low (high) Y_p is significantly increased (suppressed); a more detailed description can be found in EM (see Fig. 5).

Figure 4 reports the r -process yields for the 5- ν scenario (red line) and for the 3- ν scenario (blue line), comparing

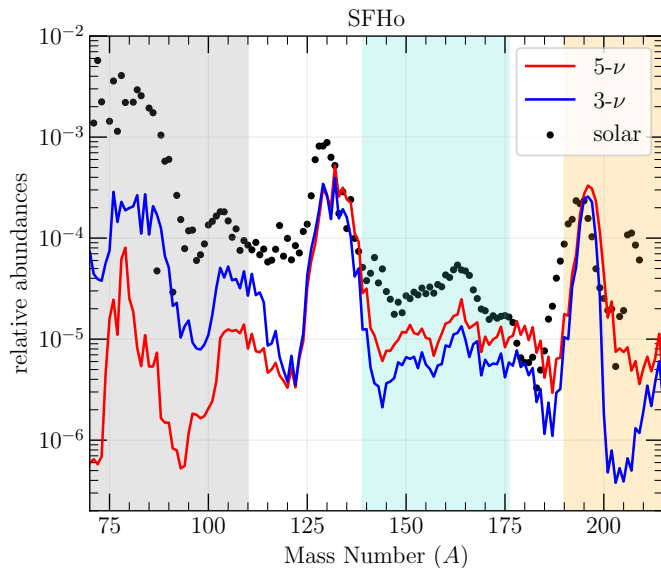


FIG. 4. Comparison between the solar relative abundances (black filled circles) as a function of the mass number A and the nucleosynthetic yields from the 5ν (red line) and the 3ν (blue line) scenarios; both abundances are rescaled to match at $A = 132$. Note the better match with data for lanthanides $139 < A < 176$ (blue-shaded region) and for very heavy elements with $190 < A < 215$ (orange shaded); very light elements with $70 < A < 110$ (grey shaded) are significantly suppressed.

them to the abundances measured in the solar system (filled black circles). When comparing the two scenarios, it is apparent that the inclusion of five neutrino species leads to larger abundances of lanthanides, i.e., with mass number $139 < A < 176$ (blue-shaded region), and to almost an order of magnitude larger yields for elements with $190 < A < 215$ (orange-shaded region)¹. At the same time, elements with $70 < A < 110$ are significantly suppressed (grey shaded). Hence, our results for the SFHo EOS clearly indicate that inclusion of muonic interactions provides a $\sim 100\%$ increase in the yields of lanthanides, thus resolving naturally a significant tension that numerical simulations have so far encountered within the standard three-species scenario. While promising, our findings also come with a caveat. Specifically, simulations carried out with the stiffer DD2 EOS, which is only marginally consistent with astronomical constraints [68], indicate that the differences in the lanthanides yields are much smaller (see Fig. 6 in SM). This different behavior is rooted in many factors: lower temperatures and densities producing weaker shocks for the DD2 EOS [69], significantly less ejected matter and weaker muonization, and, more importantly, a smaller reduction of Y_p in post-merger, at least over the timescales explored. We conjecture that muonic interac-

tions may require longer timescales to boost lanthanide production in stiff EOSs and plan to explore such scenarios in future works.

Conclusions. We have presented the first GRMHD simulations of BNS mergers employing a moment-based, energy-integrated approach to describe the radiative transport via five neutrino species with μ^- , μ^+ and muonic β -processes based on full kinematic calculations and medium modifications in the nucleon propagator for hadronic currents. Because our focus is on the effects of muonic interactions, we have considered binary systems described by two distinct temperature-dependent EOSs and a total mass that would yield a long-lived remnant. Importantly, the simulations are contrasted with twin simulations that use the same initial data and computational infrastructure, but are based on the traditional three neutrino-species approach to account for radiative losses.

Our results reveal that while an $np\mu\nu$ -equilibrium, similar to an $npe\nu$ -equilibrium, is established within a few milliseconds post-merger, the unique properties of muons and out-of-weak-equilibrium potentials are such that a significant de-muonization occurs in low-density, low-temperature regions after the merger. The creation of μ^- - μ^+ pairs and the muonization in the heated regions right after the merger, together with a more intense initial neutrino emission, lead to a cooler remnant and disk. Muonic-interaction channels require a significant amount of energy, which would be otherwise tapped by electronic β -processes to drive protonization of the ejecta and disk, leading to an overall reduction of ν_e -reabsorption and $\bar{\nu}_e$ emission. Together with the changed hierarchy of trapped neutrinos and competition between muonic and electronic processes, these factors result in a weaker protonization and a more neutron-rich ejection of matter over dynamical timescales. In turn, this naturally boosts lanthanide production and suppresses the formation of lighter elements via r -process nucleosynthesis. The importance of this result comes from the fact that present state-of-the-art simulations with three neutrino species report the overproduction of proton-rich matter that inevitably leads to a premature blue-kilonova component due to excessive electronization [3, 22, 31, 70]. Hence, our results show the necessity to include (anti)muons and muonic weak interactions to accurately capture post-merger dynamics, ejecta composition, and nucleosynthesis yields.

While being the first calculations of this type, our simulations also come with some limitations. First, they neglect the presence of a dynamically important magnetic field that could influence the dynamics of the remnant and of the ejecta [39, 71–77]. Second, because of unaccounted leptonic weak interactions that convert $\mu^{-/+}$ to $e^{-/+}$ [50–52], a lack of realistic spectral blocking for pair processes, and a weakened (de-)muonization for stiff-EOSs, our approach may (slightly) overproduce heavy elements. Finally, the evidence of positive values for the out-of-weak-equilibrium chemical potential μ_{Δ}^{npe} indicates that a secular electronization is expected to take place on timescales much longer than those explored here. These considerations calls for both efficient

¹ We also find an 18% better match in the actinides range ($232 < A < 238$), not reported in Fig. 4 because of the large uncertainty in the solar data.

long-term post-merger GRMHD evolution methods [33], with spectral neutrino transport [34, 47], and kernel-based weak interactions [42, 48, 51, 78], some of which will be discussed in an upcoming publication [79].

Acknowledgments. It is a pleasure to thank L. Baccioli, R. Bollig, T. Fischer, T. Janka, and D. Radice for useful discussions. Support comes from the State of Hesse within the Research Cluster ELEMENTS (Project ID 500/10.006) and through the European Research Council Advanced Grant “JETSET: Launching, propagation and emission of relativistic jets from binary mergers and across mass scales” (grant No. 884631). LR acknowledges the Walter Greiner Gesellschaft zur Förderung der physikalischen Grundlagenforschung e.V. through the Carl W. Fueck Laureatus Chair. ST acknowledges support from NASA award ATP-80NSSC22K1898. The calculations were performed in part on the local ITP Supercomputing Clusters Iboga and Calea and in part on HPE Apollo HAWK at the High Performance Computing Center Stuttgart (HLRS) under the grants BNSMIC and BBHDISKS.

-
- [1] L. Baiotti and L. Rezzolla, Binary neutron-star mergers: a review of Einstein’s richest laboratory, *Rept. Prog. Phys.* **80**, 096901 (2017), arXiv:1607.03540 [gr-qc].
- [2] V. Paschalidis, General relativistic simulations of compact binary mergers as engines for short gamma-ray bursts, *Classical and Quantum Gravity* **34**, 084002 (2017), arXiv:1611.01519 [astro-ph.HE].
- [3] B. D. Metzger, Kilonovae, *Living Reviews in Relativity* **20**, 3 (2017), arXiv:1610.09381 [astro-ph.HE].
- [4] A. Arcones and F.-K. Thielemann, Origin of the elements, *Astronomy and Astrophysics Reviews* **31**, 1 (2023).
- [5] S. Rosswog, M. Liebendörfer, F.-K. Thielemann, M. B. Davies, W. Benz, and T. Piran, Mass ejection in neutron star mergers, *Astron. Astrophys.* **341**, 499 (1999), astro-ph/9811367.
- [6] L. Dessart, C. D. Ott, A. Burrows, S. Rosswog, and E. Livne, Neutrino Signatures and the Neutrino-Driven Wind in Binary Neutron Star Mergers, *Astrophys. J.* **690**, 1681 (2009), arXiv:0806.4380.
- [7] L. Rezzolla, L. Baiotti, B. Giacomazzo, D. Link, and J. A. Font, Accurate evolutions of unequal-mass neutron-star binaries: properties of the torus and short GRB engines, *Class. Quantum Grav.* **27**, 114105 (2010), arXiv:1001.3074 [gr-qc].
- [8] L. F. Roberts, D. Kasen, W. H. Lee, and E. Ramirez-Ruiz, Electromagnetic Transients Powered by Nuclear Decay in the Tidal Tails of Coalescing Compact Binaries, *Astrophys. J. Lett.* **736**, L21 (2011), arXiv:1104.5504 [astro-ph.HE].
- [9] K. Kyutoku, K. Ioka, and M. Shibata, Ultrarelativistic electromagnetic counterpart to binary neutron star mergers, *Mon. Not. R. Astron. Soc.* **437**, L6 (2014), arXiv:1209.5747 [astro-ph.HE].
- [10] S. Rosswog, The dynamic ejecta of compact object mergers and eccentric collisions, *Royal Society of London Philosophical Transactions Series A* **371**, 20272 (2013), arXiv:1210.6549 [astro-ph.HE].
- [11] A. Bauswein, S. Goriely, and H.-T. Janka, Systematics of Dynamical Mass Ejection, Nucleosynthesis, and Radioactively Powered Electromagnetic Signals from Neutron-star Mergers, *Astrophys. J.* **773**, 78 (2013), arXiv:1302.6530 [astro-ph.SR].
- [12] K. Hotokezaka, K. Kiuchi, K. Kyutoku, H. Okawa, Y.-i. Sekiguchi, M. Shibata, and K. Taniguchi, Mass ejection from the merger of binary neutron stars, *Phys. Rev. D* **87**, 024001 (2013), arXiv:1212.0905 [astro-ph.HE].
- [13] F. Foucart, M. B. Deaton, M. D. Duez, E. O’Connor, C. D. Ott, R. Haas, L. E. Kidder, H. P. Pfeiffer, M. A. Scheel, and B. Szilagy, Neutron star-black hole mergers with a nuclear equation of state and neutrino cooling: Dependence in the binary parameters, *Phys. Rev. D* **90**, 024026 (2014), arXiv:1405.1121 [astro-ph.HE].
- [14] A. Perego, S. Rosswog, R. M. Cabezon, O. Korobkin, R. Käppeli, A. Arcones, and M. Liebendörfer, Neutrino-driven winds from neutron star merger remnants, *Mon. Not. R. Astron. Soc.* **443**, 3134 (2014), arXiv:1405.6730 [astro-ph.HE].
- [15] O. Just, A. Bauswein, R. A. Pulpillo, S. Goriely, and H.-T. Janka, Comprehensive nucleosynthesis analysis for ejecta of compact binary mergers, *Mon. Not. R. Astron. Soc.* **448**, 541 (2015), arXiv:1406.2687 [astro-ph.SR].
- [16] D. Martin, A. Perego, A. Arcones, F.-K. Thielemann, O. Korobkin, and S. Rosswog, Neutrino-driven Winds in the Aftermath of a Neutron Star Merger: Nucleosynthesis and Electromagnetic Transients, *Astrophys. J.* **813**, 2 (2015), arXiv:1506.05048 [astro-ph.SR].
- [17] D. Radice, F. Galeazzi, J. Lippuner, L. F. Roberts, C. D. Ott, and L. Rezzolla, Dynamical Mass Ejection from Binary Neutron Star Mergers, *Mon. Not. R. Astron. Soc.* **460**, 3255 (2016), arXiv:1601.02426 [astro-ph.HE].
- [18] L. Lehner, S. L. Liebling, C. Palenzuela, O. L. Caballero, E. O’Connor, M. Anderson, and D. Neilsen, Unequal mass binary neutron star mergers and multimessenger signals, *Classical and Quantum Gravity* **33**, 184002 (2016), arXiv:1603.00501 [gr-qc].
- [19] T. Dietrich and M. Ujevic, Modeling dynamical ejecta from binary neutron star mergers and implications for electromagnetic counterparts, *Classical and Quantum Gravity* **34**, 105014 (2017), arXiv:1612.03665 [gr-qc].
- [20] S. Fujibayashi, Y. Sekiguchi, K. Kiuchi, and M. Shibata, Properties of neutrino-driven ejecta from the remnant of a binary neutron star merger: Pure radiation hydrodynamics case, *The Astrophysical Journal* **846**, 114 (2017).
- [21] L. Bovard, D. Martin, F. Guercilena, A. Arcones, L. Rezzolla, and O. Korobkin, On r-process nucleosynthesis from matter ejected in binary neutron star mergers, *Phys. Rev. D* **96**, 124005 (2017), arXiv:1709.09630 [gr-qc].
- [22] K. Kawaguchi, M. Shibata, and M. Tanaka, Radiative Transfer Simulation for the Optical and Near-infrared Electromagnetic Counterparts to GW170817, *Astrophys. J. Lett.* **865**, L21 (2018), arXiv:1806.04088 [astro-ph.HE].
- [23] S. Bernuzzi, F. Magistrelli, M. Jacobi, D. Logoteta, A. Perego, and D. Radice, Long-lived neutron-star remnants from asymmetric binary neutron star mergers: element formation, kilonova signals and gravitational waves, arXiv preprint arXiv:2409.18185 (2024).
- [24] D. Kasen, B. Metzger, J. Barnes, E. Quataert, and E. Ramirez-Ruiz, Origin of the heavy elements in binary neutron-star mergers from a gravitational-wave event, *Nature* **551**, 80 (2017), arXiv:1710.05463 [astro-ph.HE].
- [25] S. Rosswog, J. Sollerman, U. Feindt, A. Goobar, O. Korobkin, R. Wollaeger, C. Fremling, and M. M. Kasliwal, The first direct double neutron star merger detection: implications for cosmic nucleosynthesis, *Astron. Astrophys.* **615**, A132 (2018), arXiv:1710.05445 [astro-ph.HE].

- [26] I. Arcavi, G. Hosseinzadeh, D. A. Howell, C. McCully, D. Poznanski, D. Kasen, J. Barnes, M. Zaltzman, S. Vasylyev, D. Maoz, and S. Valenti, Optical emission from a kilonova following a gravitational-wave-detected neutron-star merger, *Nature* **551**, 64 (2017), arXiv:1710.05843 [astro-ph.HE].
- [27] R. Chornock and *et al.*, The Electromagnetic Counterpart of the Binary Neutron Star Merger LIGO/Virgo GW170817. IV. Detection of Near-infrared Signatures of r-process Nucleosynthesis with Gemini-South, *Astrophys. J. Letters* **848**, L19 (2017), arXiv:1710.05454 [astro-ph.HE].
- [28] N. R. Tanvir, A. J. Levan, C. González-Fernández, O. Korobkin, I. Mandel, S. Rosswog, J. Hjorth, P. D’Avanzo, A. S. Fruchter, C. L. Fryer, T. Kangas, B. Milvang-Jensen, S. Rosetti, D. Steeghs, R. T. Wollaeger, Z. Cano, C. M. Copperwheat, and R. A. M. J. Wijers, The Emergence of Two Lanthanide-rich Kilonova Following the Merger of Two Neutron Stars, *Astrophys. J. Letters* **848**, L27 (2017), arXiv:1710.05455 [astro-ph.HE].
- [29] D. M. Siegel and B. D. Metzger, Three-Dimensional General-Relativistic Magnetohydrodynamic Simulations of Remnant Accretion Disks from Neutron Star Mergers: Outflows and r -Process Nucleosynthesis, *Physical Review Letters* **119**, 231102 (2017), arXiv:1705.05473 [astro-ph.HE].
- [30] R. Gill, A. Nathanail, and L. Rezzolla, When Did the Remnant of GW170817 Collapse to a Black Hole?, *Astrophys. J.* **876**, 139 (2019), arXiv:1901.04138 [astro-ph.HE].
- [31] K. Kawaguchi, S. Fujibayashi, N. Domoto, K. Kiuchi, M. Shibata, and S. Wanajo, Kilonovae of binary neutron star mergers leading to short-lived remnant neutron star formation, arXiv preprint arXiv:2306.06961 (2023).
- [32] K. Kiuchi, S. Fujibayashi, K. Hayashi, K. Kyutoku, Y. Sekiguchi, and M. Shibata, Self-Consistent Picture of the Mass Ejection from a One Second Long Binary Neutron Star Merger Leaving a Short-Lived Remnant in a General-Relativistic Neutrino-Radiation Magnetohydrodynamic Simulation, *Phys. Rev. Lett.* **131**, 011401 (2023), arXiv:2211.07637 [astro-ph.HE].
- [33] H. H.-Y. Ng, J.-L. Jiang, C. Musolino, C. Ecker, S. D. Tootle, and L. Rezzolla, Hybrid approach to long-term binary neutron-star simulations, *Phys. Rev. D* **109**, 064061 (2024), arXiv:2312.11358 [gr-qc].
- [34] F. Foucart, M. D. Duez, F. Hebert, L. E. Kidder, H. P. Pfeiffer, and M. A. Scheel, Monte-Carlo Neutrino Transport in Neutron Star Merger Simulations, *Astrophys. J. Lett.* **902**, L27 (2020), arXiv:2008.08089 [astro-ph.HE].
- [35] F. Zappa, S. Bernuzzi, D. Radice, and A. Perego, Binary neutron star merger simulations with neutrino transport and turbulent viscosity: impact of different schemes and grid resolution, *Mon. Not. R. Astron. Soc.* **520**, 1481 (2023), arXiv:2210.11491 [astro-ph.HE].
- [36] P. C.-K. Cheong, F. Foucart, M. D. Duez, A. Offermans, N. Muhammed, and P. Chawhan, Energy-dependent and Energy-integrated Two-moment General-relativistic Neutrino Transport Simulations of a Hypermassive Neutron Star, *Astrophys. J.* **975**, 116 (2024), arXiv:2407.16017 [astro-ph.HE].
- [37] F. Foucart, P. C.-K. Cheong, M. D. Duez, L. E. Kidder, H. P. Pfeiffer, and M. A. Scheel, Robustness of neutron star merger simulations to changes in neutrino transport and neutrino-matter interactions, *Phys. Rev. D* **110**, 083028 (2024), arXiv:2407.15989 [astro-ph.HE].
- [38] R. Ciolfi, Collimated outflows from long-lived binary neutron star merger remnants, *Monthly Notices of the Royal Astronomical Society: Letters* **495**, L66 (2020).
- [39] L. Combi and D. M. Siegel, Jets from neutron-star merger remnants and massive blue kilonovae, *Phys. Rev. Lett.* **131**, 231402 (2023).
- [40] C. Musolino, L. Rezzolla, and E. R. Most, On the impact of neutrinos on the launching of relativistic jets from “magnetars” produced in neutron-star mergers, arXiv e-prints , arXiv:2410.06253 (2024), arXiv:2410.06253 [astro-ph.HE].
- [41] D. Radice, S. Bernuzzi, A. Perego, and R. Haas, A new moment-based general-relativistic neutrino-radiation transport code: Methods and first applications to neutron star mergers, *Mon. Not. Roy. Astron. Soc.* **512**, 1499 (2022), arXiv:2111.14858 [astro-ph.HE].
- [42] R. Bollig, H. T. Janka, A. Lohs, G. Martínez-Pinedo, C. J. Horowitz, and T. Melson, Muon Creation in Supernova Matter Facilitates Neutrino-Driven Explosions, *Phys. Rev. Lett.* **119**, 242702 (2017), arXiv:1706.04630 [astro-ph.HE].
- [43] E. Loffredo, A. Perego, D. Logoteta, and M. Branchesi, Muons in the aftermath of neutron star mergers and their impact on trapped neutrinos, *Astronomy and Astrophysics* **672**, A124 (2023), arXiv:2209.04458 [astro-ph.HE].
- [44] H. Gieg, F. Schianchi, M. Ujevic, and T. Dietrich, On the Role of Muons in Binary Neutron Star Mergers: First Simulations, arXiv e-prints (2024), arXiv:2409.04420 [gr-qc].
- [45] C. Musolino and L. Rezzolla, A practical guide to a moment approach for neutrino transport in numerical relativity, *Mon. Not. R. Astron. Soc.* **528**, 5952 (2024), arXiv:2304.09168 [gr-qc].
- [46] P. C.-K. Cheong, A. T.-L. Lam, H. H.-Y. Ng, and T. G. F. Li, Gmunu: paralleled, grid-adaptive, general-relativistic magnetohydrodynamics in curvilinear geometries in dynamical space-times, *Monthly Notices of the Royal Astronomical Society* **508**, 2279 (2021), <https://academic.oup.com/mnras/article-pdf/508/2/2279/40566816/stab2606.pdf>.
- [47] P. C.-K. Cheong, H. H.-Y. Ng, A. T.-L. Lam, and T. G. F. Li, General-relativistic radiation transport scheme in gmunu. i. implementation of two-moment-based multifrequency radiative transfer and code tests, *The Astrophysical Journal Supplement Series* **267**, 38 (2023).
- [48] H. H.-Y. Ng, P. C.-K. Cheong, A. T.-L. Lam, and T. G. F. Li, General-relativistic radiation transport scheme in gmunu. ii. implementation of novel microphysical library for neutrino radiation—weakhub, *The Astrophysical Journal Supplement Series* **272**, 9 (2024).
- [49] R. Ardevol-Pulpillo, H. T. Janka, O. Just, and A. Bauswein, Improved leakage-equilibration-absorption scheme (ILEAS) for neutrino physics in compact object mergers, *Mon. Not. R. Astron. Soc.* , 601 (2019), arXiv:1808.00006 [astro-ph.HE].
- [50] A. Lohs, *Neutrino Reactions in Hot and Dense Matter*, Ph.D. thesis, Technische Universität (2015).
- [51] T. Fischer, G. Guo, G. Martínez-Pinedo, M. Liebendörfer, and A. Mezzacappa, Muonization of supernova matter, *Physical Review D* **102**, 123001 (2020).
- [52] G. Guo, G. Martínez-Pinedo, A. Lohs, and T. Fischer, Charged-current muonic reactions in core-collapse supernovae, *Physical Review D* **102**, 023037 (2020).
- [53] E. O’Connor, An Open-source Neutrino Radiation Hydrodynamics Code for Core-collapse Supernovae, *Astrophys. J., Supp.* **219**, 24 (2015), arXiv:1411.7058 [astro-ph.HE].
- [54] M. Hempel and J. Schaffner-Bielich, A statistical model for a complete supernova equation of state, *Nuclear Physics A* **837**, 210 (2010), arXiv:0911.4073 [nucl-th].
- [55] S. Typel, G. Ropke, T. Klahn, D. Blaschke, and H. H. Wolter, Composition and thermodynamics of nuclear matter with light clusters, *Phys. Rev. C* **81**, 015803 (2010), arXiv:0908.2344

- [nucl-th].
- [56] L. J. Papenfort, S. D. Tootle, P. Grandclément, E. R. Most, and L. Rezzolla, New public code for initial data of unequal-mass, spinning compact-object binaries, *Phys. Rev. D* **104**, 024057 (2021).
- [57] S. D. Tootle, L. J. Papenfort, E. R. Most, and L. Rezzolla, Quasi-universal Behavior of the Threshold Mass in Unequal-mass, Spinning Binary Neutron Star Mergers, *Astrophys. J. Lett.* **922**, L19 (2021), arXiv:2109.00940 [gr-qc].
- [58] M. A. Pajkos and E. R. Most, The Influence of Muons, Pions, and Trapped Neutrinos on Neutron Star Mergers, arXiv e-prints (2024), arXiv:2409.09147 [astro-ph.HE].
- [59] S. Tootle, C. Ecker, K. Topolski, T. Demircik, M. Järvinen, and L. Rezzolla, Quark formation and phenomenology in binary neutron-star mergers using V-QCD, *SciPost Phys.* **13**, 109 (2022), arXiv:2205.05691 [astro-ph.HE].
- [60] K. Topolski, S. Tootle, and L. Rezzolla, Black hole - neutron star binaries with high spins and large mass asymmetries: II. Properties of dynamical simulations, arXiv e-prints, arXiv:2409.06777 (2024), arXiv:2409.06777 [gr-qc].
- [61] P. L. Espino, P. Hammond, D. Radice, S. Bernuzzi, R. Gamba, F. Zappa, L. F. L. Micchi, and A. Perego, Neutrino Trapping and Out-of-Equilibrium Effects in Binary Neutron-Star Merger Remnants, *Phys. Rev. Lett.* **132**, 211001 (2024), arXiv:2311.00031 [astro-ph.HE].
- [62] L. Rezzolla and K. Takami, Gravitational-wave signal from binary neutron stars: A systematic analysis of the spectral properties, *Phys. Rev. D* **93**, 124051 (2016), arXiv:1604.00246 [gr-qc].
- [63] A. Perego, S. Bernuzzi, and D. Radice, Thermodynamics conditions of matter in neutron star mergers, *Eur. Phys. J. A* **55**, 124 (2019), arXiv:1903.07898 [gr-qc].
- [64] L. Bovard and L. Rezzolla, On the use of tracer particles in simulations of binary neutron stars, *Classical and Quantum Gravity* **34**, 215005 (2017), arXiv:1705.07882 [gr-qc].
- [65] D. M. Siegel, R. Ciolfi, and L. Rezzolla, Magnetically Driven Winds from Differentially Rotating Neutron Stars and X-Ray Afterglows of Short Gamma-Ray Bursts, *Astrophys. J.* **785**, L6 (2014), arXiv:1401.4544 [astro-ph.HE].
- [66] C. Musolino, R. Duqué, and L. Rezzolla, “Extended Emission” from fallback accretion onto merger remnants, *Astrophys. J. Lett.* **966**, L31 (2024), arXiv:2402.11009 [astro-ph.HE].
- [67] M. Hanauske, K. Takami, L. Bovard, L. Rezzolla, J. A. Font, F. Galeazzi, and H. Stöcker, Rotational properties of hypermassive neutron stars from binary mergers, *Phys. Rev. D* **96**, 043004 (2017), arXiv:1611.07152 [gr-qc].
- [68] E. R. Most, L. R. Weih, L. Rezzolla, and J. Schaffner-Bielich, New Constraints on Radii and Tidal Deformabilities of Neutron Stars from GW170817, *Phys. Rev. Lett.* **120**, 261103 (2018), arXiv:1803.00549 [gr-qc].
- [69] P. L. Espino, D. Radice, F. Zappa, R. Gamba, and S. Bernuzzi, Impact of moment-based, energy integrated neutrino transport on microphysics and ejecta in binary neutron star mergers, *Phys. Rev. D* **109**, 103027 (2024), arXiv:2311.12923 [astro-ph.HE].
- [70] S. Fujibayashi, K. Kiuchi, N. Nishimura, Y. Sekiguchi, and M. Shibata, Mass ejection from the remnant of a binary neutron star merger: Viscous-radiation hydrodynamics study, *The Astrophysical Journal* **860**, 64 (2018).
- [71] R. Ciolfi, Collimated outflows from long-lived binary neutron star merger remnants, *Mon. Not. R. Astron. Soc.* **495**, L66 (2020), arXiv:2001.10241 [astro-ph.HE].
- [72] P. Mösta, D. Radice, R. Haas, E. Schnetter, and S. Bernuzzi, A magnetar engine for short GRBs and kilonovae, *Astrophys. J. Lett.* **901**, L37 (2020), arXiv:2003.06043 [astro-ph.HE].
- [73] M. Chabanov, S. D. Tootle, E. R. Most, and L. Rezzolla, Crustal Magnetic Fields Do Not Lead to Large Magnetic-field Amplifications in Binary Neutron Star Mergers, *Astrophys. J. Lett.* **945**, L14 (2023), arXiv:2211.13661 [astro-ph.HE].
- [74] E. R. Most and E. Quataert, Flares, Jets, and Quasiperiodic Outbursts from Neutron Star Merger Remnants, *Astrophys. J. Lett.* **947**, L15 (2023), arXiv:2303.08062 [astro-ph.HE].
- [75] K. Kiuchi, A. Reboul-Salze, M. Shibata, and Y. Sekiguchi, A large-scale magnetic field produced by a solar-like dynamo in binary neutron star mergers, *Nature Astronomy* **8**, 298 (2024), arXiv:2306.15721 [astro-ph.HE].
- [76] J. Bamber, A. Tsokaros, M. Ruiz, and S. L. Shapiro, Jetlike structures in low-mass binary neutron star merger remnants, *Phys. Rev. D* **110**, 024046 (2024), arXiv:2405.03705 [astro-ph.HE].
- [77] R. Aguilera-Miret, C. Palenzuela, F. Carrasco, S. Rosswog, and D. Viganò, Delayed jet launching in binary neutron star mergers with realistic initial magnetic fields, *Phys. Rev. D* **110**, 083014 (2024), arXiv:2407.20335 [astro-ph.HE].
- [78] P. C.-K. Cheong, F. Foucart, H. H.-Y. Ng, A. Offermans, M. D. Duez, N. Muhammed, and P. Chawhan, Influence of neutrino-electron scattering and neutrino-pair annihilation on hypermassive neutron star, arXiv e-prints (2024), arXiv:2410.20681 [astro-ph.HE].
- [79] J.-L. Jiang, H. H.-Y. Ng, M. Chabanov, and L. Rezzolla, Long-term impact of magnetic-field strength on the evolution and electromagnetic emission from neutron-star merger remnants, in preparation (2024).
- [80] R. Haas and *et al.*, *The Einstein Toolkit* (2020), to find out more, visit <http://einstein toolkit.org>.
- [81] Z. B. Etienne, V. Paschalidis, R. Haas, P. Mösta, and S. L. Shapiro, IllinoisGRMHD: an open-source, user-friendly GRMHD code for dynamical spacetimes, *Class. Quantum Grav.* **32**, 175009 (2015), arXiv:1501.07276 [astro-ph.HE].
- [82] E. R. Most, L. J. Papenfort, and L. Rezzolla, Beyond second-order convergence in simulations of magnetized binary neutron stars with realistic microphysics, *Mon. Not. R. Astron. Soc.* **490**, 3588 (2019), arXiv:1907.10328 [astro-ph.HE].
- [83] P. Londrillo and L. Del Zanna, On the divergence-free condition in godunov-type schemes for ideal magnetohydrodynamics: the upwind constrained transport method, *Journal of Computational Physics* **195**, 17 (2004).
- [84] Z. B. Etienne, Y. T. Liu, and S. L. Shapiro, Relativistic magnetohydrodynamics in dynamical spacetimes: A new adaptive mesh refinement implementation, *Phys. Rev. D* **82**, 084031 (2010), arXiv:1007.2848 [astro-ph.HE].
- [85] S. Bernuzzi and D. Hilditch, Constraint violation in free evolution schemes: comparing BSSNOK with a conformal decomposition of Z4, *Phys. Rev. D* **81**, 084003 (2010), arXiv:0912.2920 [gr-qc].
- [86] D. Alic, C. Bona-Casas, C. Bona, L. Rezzolla, and C. Palenzuela, Conformal and covariant formulation of the Z4 system with constraint-violation damping, *Phys. Rev. D* **85**, 064040 (2012), arXiv:1106.2254 [gr-qc].
- [87] E. R. Most, L. J. Papenfort, V. Dexheimer, M. Hanauske, S. Schramm, H. Stöcker, and L. Rezzolla, Signatures of quark-hadron phase transitions in general-relativistic neutron-star mergers, *Phys. Rev. Lett.* **122**, 061101 (2019), arXiv:1807.03684 [astro-ph.HE].
- [88] E. R. Most, L. Jens Papenfort, V. Dexheimer, M. Hanauske, H. Stöcker, and L. Rezzolla, On the deconfinement phase transition in neutron-star mergers, *Eur. Phys. J. A* **56**, 59

- (2020), [arXiv:1910.13893 \[astro-ph.HE\]](#).
- [89] C. Horowitz, Weak magnetism for antineutrinos in supernovae, *Physical Review D* **65**, 043001 (2002).
- [90] T. Hobbs, M. Alberg, and G. A. Miller, Role of nucleon strangeness in supernova explosions, *Physical Review C* **93**, 052801 (2016).
- [91] A. Burrows, S. Reddy, and T. A. Thompson, Neutrino opacities in nuclear matter, *Nuclear Physics A* **777**, 356 (2006), [astro-ph/0404432](#).
- [92] R. G. Bollig, *Muon Creation and Effects in Supernovae*, Ph.D. thesis, Technische Universität München (2018).
- [93] D. W. Neilsen, S. L. Liebling, M. Anderson, L. Lehner, E. O'Connor, and C. Palenzuela, Magnetized neutron stars with realistic equations of state and neutrino cooling, *Phys. Rev. D* **89**, 104029 (2014), [arXiv:1403.3680 \[gr-qc\]](#).
- [94] H. Zhao, A fast sweeping method for eikonal equations, *Mathematics of computation* **74**, 603 (2005).
- [95] D. Radice, A. Perego, K. Hotokezaka, S. A. Fromm, S. Bernuzzi, and L. F. Roberts, Binary Neutron Star Mergers: Mass Ejection, Electromagnetic Counterparts, and Nucleosynthesis, *Astrophys. J.* **869**, 130 (2018), [arXiv:1809.11161 \[astro-ph.HE\]](#).
- [96] J. Lippuner and L. F. Roberts, r-process Lanthanide Production and Heating Rates in Kilonovae, *Astrophys. J.* **815**, 82 (2015), [arXiv:1508.03133 \[astro-ph.HE\]](#).
- [97] J. Lippuner and L. F. Roberts, SkyNet: A Modular Nuclear Reaction Network Library, *Astrophys. J., Supp.* **233**, 18 (2017), [arXiv:1706.06198 \[astro-ph.HE\]](#).
- [98] L. J. Papenfort, R. Gold, and L. Rezzolla, Dynamical ejecta and nucleosynthetic yields from eccentric binary neutron-star mergers, *Phys. Rev. D* **98**, 104028 (2018), [arXiv:1807.03795 \[gr-qc\]](#).
- [99] R. H. Cyburt, A. M. Amthor, R. Ferguson, Z. Meisel, K. Smith, S. Warren, A. Heger, R. D. Hoffman, T. Rauscher, A. Sakharuk, H. Schatz, F. K. Thielemann, and M. Wiescher, The JINA REACLIB Database: Its Recent Updates and Impact on Type-I X-ray Bursts, *Astrophys. J., Supp.* **189**, 240 (2010).
- [100] I. V. Panov, I. Y. Korneev, T. Rauscher, G. Martínez-Pinedo, A. Kelić-Heil, N. T. Zinner, and F.-K. Thielemann, Neutron-induced astrophysical reaction rates for translead nuclei, *Astron. Astrophys.* **513**, A61 (2010).

END MATTER

Numerical methods and setup. We perform our simulations within the general-relativistic ideal-magnetohydrodynamics (GRMHD) approximation with adaptive-mesh-refinement provided by the `EinsteinToolkit` [80]. The GRMHD equations are solved with fourth-order accurate finite differences by the `FIL` code [81, 82] and the divergence-free constraint of the magnetic field is ensured via constrained transport evolution of the magnetic vector potential [83, 84]. `FIL` provides its own spacetime evolution code `Antelope` based on the `Z4` system [85, 86], as well as a framework for handling temperature and composition-dependent equations of state (EOSs) [87, 88]. High-quality initial data for our binaries is obtained with the `FUKA` solver [56, 57]. `FIL-M1` [45] provides an energy-integrated, moment-based M1 scheme that has so far considered three neutrino species (electron neutrinos ν_e , electron antineutrinos $\bar{\nu}_e$, and a collective species describing muon neutrinos ν_μ , tau neutrinos ν_τ and the corresponding antineutrinos ν_x) with conventional neutrino opacities for leading-order weak interactions. As anticipated, we have extended `FIL-M1` to evolve five neutrino species, with the addition of ν_μ and $\bar{\nu}_\mu$, while ν_τ and $\bar{\nu}_\tau$ are evolved as an effective species ν_x since β -processes involving them are negligible due to the high rest-mass of the tau particle (1776.9 MeV).

Extensions were also needed for the GRMHD equations and EOS modules to handle self-consistently the presence of muons in the simulations and the neutrino transport with the five neutrino species. In particular, the EOS module has been enhanced with the addition of a leptonic table accounting for pressure, internal energy and specific-entropy contributions to the nuclear EOS based on an ideal Fermi gas of μ^- (μ^+) and e^- (e^+), where the electron fraction Y_e and muon fraction Y_μ are sampled within $[0.01, 0.5]$ linearly and $[5 \times 10^{-4}, 0.2]$ logarithmically, respectively. This table is then used in conjunction with the conventional nuclear EOS table where the charge fraction is the fraction of protons $Y_p = Y_e + Y_\mu$. Finally, the muon fraction is then advected by `FIL-M1`

$$\partial_t(\sqrt{\gamma}\rho W Y_\mu) + \partial_i(\sqrt{\gamma}\rho u^i Y_\mu) = -\mathcal{N}_{Y_\mu}, \quad (1)$$

where u^α is the fluid four velocity, W is Lorentz factor and $\mathcal{N}_{Y_\mu} := m_b (\mathcal{N}_{\nu_\mu} - \mathcal{N}_{\bar{\nu}_\mu})$ is the collisional source term of the net muon flavor neutrino number density, and m_b is the rest-mass of a baryon. The conservative to primitive inversion and atmospheric treatment routines were also updated to accommodate the additional degree of freedom while ensuring lepton number conservation.

The set of weak interactions. Table I summarizes the weak interactions included in this work. Note that the pair processes (e), (f), and (g) are applied exclusively to heavy-lepton neutrinos and are computed on-the-fly during the simulation using Eqs. (B24)–(B32) from Ref. [49]. Furthermore: in reac-

tion (g) accounts only for massive photons in the transverse mode [48]; the neutrino-nucleon elastic scattering (i) incorporates nucleon recoil, weak magnetism [89], strangeness in the axial coupling ($g_A^s = -0.1$) [90], and virial corrections at low densities; the neutrino-nuclei scattering (h), includes the effects of Coulomb interactions, electron polarization, and nuclear form factors [91].

(a) $\nu_e + n \leftrightarrow p + e^-$	(e) $N + N \leftrightarrow N + N + \nu_{\mu/\tau} + \bar{\nu}_{\mu/\tau}$
(b) $\bar{\nu}_e + p \leftrightarrow n + e^+$	(f) $e^- + e^+ \leftrightarrow \nu_{\mu/\tau} + \bar{\nu}_{\mu/\tau}$
(c) $\nu_\mu + n \leftrightarrow p + \mu^-$	(g) $\gamma_T \leftrightarrow \nu_{\mu/\tau} + \bar{\nu}_{\mu/\tau}$
(d) $\bar{\nu}_\mu + p \leftrightarrow n + \mu^+$	(h) $\nu_i + A \leftrightarrow \nu_i + A$
	(i) $\nu_i + N \leftrightarrow \nu_i + N$

TABLE I. Weak interactions from `WeakHub` considered in this work [48]. Here, A refers to heavy nuclei including light clusters such as α -particles and 2H , N represents either a proton or a neutron, while ν_i is any neutrino species.

Strategies to prevent artificial over (de-)muonization. When $\mu_e \leq m_\mu$, initial data in both $np\mu$ and npe equilibria must abandon the $np\mu$ -equilibrium condition by setting $Y_\mu = 0$ to asymptotically satisfy npe -equilibrium, thus matching composition in low-density, low-temperature regions without (anti)muons. This adjustment is necessary because both equilibria cannot coexist in these regions: μ_e can never equal μ_μ when Y_μ is nonzero (see Fig. 3.5 in [92]). During the evolution, unphysically high (or low) values of $\eta_{\nu_\mu}^{\text{eq}}$ (or $\eta_{\bar{\nu}_\mu}^{\text{eq}}$) [43], where $\eta_{\nu_\mu}^{\text{eq}} := (\mu_\mu + \mu_p - \mu_n)/T$ and $\eta_{\bar{\nu}_\mu}^{\text{eq}} = -\eta_{\nu_\mu}^{\text{eq}}$, arise in low-density, low-temperature regions, where $\mu_\mu \sim m_\mu$ and $Y_\mu \sim 0$. Under these conditions, and especially at the surfaces of stars during the inspiral, $\eta_{\nu_\mu}^{\text{eq}}$ can reach values $\sim 5 - 100$, causing excess μ^- production with Y_μ hitting the upper bound of the table. As argued by Ref. [92], tracking vanishing Y_μ with weak interactions for these regions is unfeasible and suitable strategies have to be designed and implemented.

In our approach, we first define a threshold Y_μ^{thr} and set $\eta_{\nu_\mu}^{\text{eq}} = \eta_{\bar{\nu}_\mu}^{\text{eq}} = 0$ in those regions where $Y_\mu < Y_\mu^{\text{thr}}$; experimentation has shown that setting $Y_\mu^{\text{thr}} = 5 \times 10^{-3}$ avoids excessive increases in the muon fraction. Furthermore, following Eq. (9.31) in Ref. [92], we apply a suppression factor based on the rest-mass density and temperature cut-offs to muonic weak interactions of the type $\mathcal{Q}' = \mathcal{Q}[1/(1 + (\rho_{\text{th}}/\rho)^5)][1/(1 + (T_{\text{th}}/T)^6)]$, where \mathcal{Q} refers to quantities such as the energy-averaged emissivities \bar{Q} , or the energy-averaged absorption opacities $\bar{\kappa}_\alpha$, and where we set $\rho_{\text{th}} := 10^{11} \text{ g cm}^{-3}$ and $T_{\text{th}} := 2.5 \text{ MeV}$.

Another issue to consider is that energy-averaged (or grey) moment schemes such as the one employed here depend on degeneracy parameters for detailed balance (Kirchhoff's law), the energy averaging of the opacities, and the rate corrections. Within 3-species approaches, it is not necessary to rescale the degeneracy parameters for ν_e and $\bar{\nu}_e$, as the small electron mass leads to a monotonic decrease in $\eta_{\nu_e}^{\text{eq}}$ as the rest-mass density reaches the atmosphere values. However, in 5-species

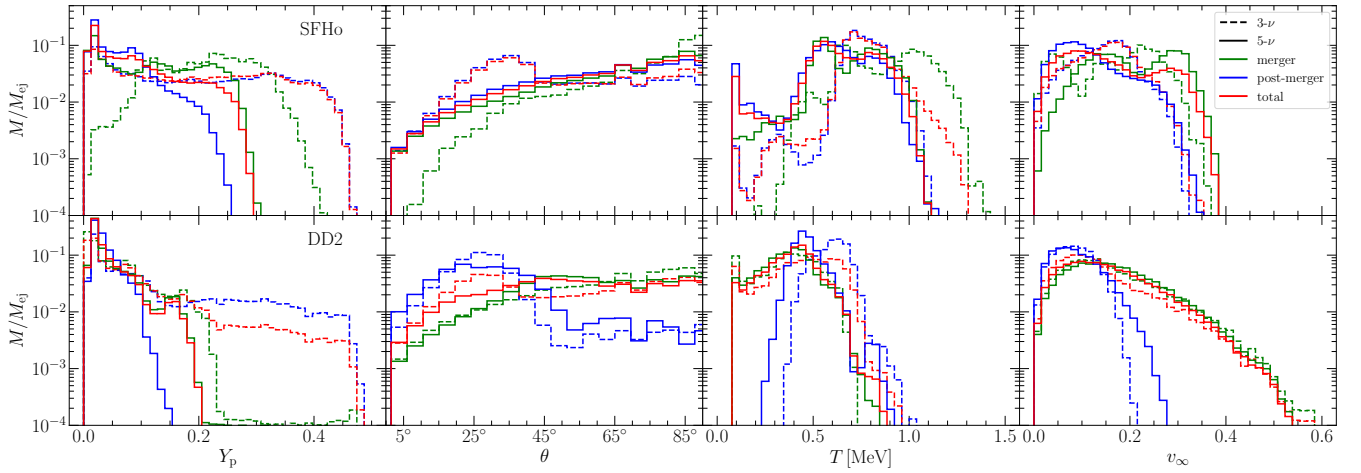


FIG. 5. Distributions of the normalized ejected mass for the 5- ν (solid lines) and 3- ν (dashed lines) scenarios, as functions (from left to right) of the proton fraction Y_p , the polar angle θ , the temperature T , and the terminal velocity v_∞ . The data is extracted on a 2-sphere at 300 km, both for the SFHo (top row) and the DD2 EOS (bottom row). Shown with red lines are the total distributions, while green and blue lines refer respectively to $\bar{t} \leq 4.0$ ms (≤ 6.5 ms) and $\bar{t} \geq 4.0$ ms (≥ 6.5 ms) for the SFHo (DD2) EOS (different times reflect the different speeds of the ejecta to reach the detector). In all cases, $Y_p \approx Y_e$, since $Y_\mu \lesssim 5 \times 10^{-3}$.

approaches, very large values of $\eta_{\nu_\mu}^{\text{eq}}$ and $\eta_{\bar{\nu}_\mu}^{\text{eq}}$ need corrections in regions where muonic interactions are negligible and $np\mu$ -equilibrium is absent. Thus, we rescale the degeneracy parameters η_ν using the optical depth τ_ν which is computed by approximately solving the Eikonal equation of $\nabla\tau_\nu(x) = \bar{\kappa}_\nu(x)$ [93] by the method of Ref. [94], where $\bar{\kappa}_\nu(x)$ is the total energy-averaged opacity as a function of spatial coordinate x . η_ν is thus expressed as $\eta_\nu = \eta_\nu^{\text{eq}}(1 - e^{-\tau_\nu})$ for all ν , and we set $\eta_i = 0$ where $\tau_i < 1$, and i only refers to ν_μ or $\bar{\nu}_\mu$.

Finally, due to the missing spectral information about the distribution function of neutrinos, attention needs to be paid with Kirchhoff’s law for pair processes (e), (f), and (g) in Table. I. A possibility is to use an approximated isotropic emissivity [53] instead of the inelastic kernels for pair processes. On the other hand, Weakhub [48] or NuLib [53] calculate the pair process spectral absorption opacity κ_a^{pp} by first computing the spectral emissivity Q^{pp} and then applying Kirchhoff’s law $\kappa_a^{\text{pp}} = Q^{\text{pp}}/\mathcal{B}(\eta_\nu^{\text{eq}})$, where $\mathcal{B}(\eta_\nu^{\text{eq}})$ is the black-body spectrum. This quantity is tabulated as an energy-averaged opacity and stored similarly to other absorption opacities. However, in low-density regions, values of $-100 \lesssim \eta_{\bar{\nu}_\mu}^{\text{eq}} \lesssim -5$ yield $\mathcal{B}(\eta_{\bar{\nu}_\mu}^{\text{eq}}) \simeq 0$ and hence excessively high values of $\kappa_{a,\bar{\nu}_\mu}^{\text{pp}}$, causing extreme de-muonization and destroying $np\mu\nu$ -equilibrium after the merger. To counter this, we calculate κ_a^{pp} on-the-fly with the fixed η_ν instead of η_ν^{eq} (alternatively, the isotropic emissivity could be tabulated and the absorption opacity be recalculated on-the-fly with η_ν).

Handling of the ejecta and their properties. To compute the r -process yields, we follow Refs. [17, 64, 95], binning the unbound fluid elements with a 40×40 grid in specific entropy s and Y_p , where the weight is given by the accumulated mass fraction. The median unbound fluid element is sampled from each non-empty bin, leading to an average number of

≈ 1000 “tracers”. We determine the dynamical timescale of the expansion of ejecta, τ , by equating the homologous evolution $\rho(t) = \rho_{\text{ext}}(v_{\text{ext}}t/r_{\text{ext}})^{-3}$, where $\rho_{\text{ext}} = 300$ km and v_{ext} are the density and velocity of the fluid element when it crosses the radius of the spherical detector r_{ext} at time t , with that obtained considering an expanding material that undergoes r -process nucleosynthesis, $\rho(t) = \rho_0(3\tau/\exp(1)t)^3$, where $\rho_0 = \rho_0(s, Y_e, 6 \text{ GK})$ [96]. The r -process yields are then computed using the nuclear-reaction network code SkyNet [97], using a workflow similar to that in Ref. [98] and the rates in Refs. [8, 99, 100]. The assumed nuclear statistical equilibrium is computed by SkyNet on the basis of the values of T , s , and Y_p of each tracer, where the rest-mass density evolution consists of an exponential decrease transitioning to an homologous expansion for $t \geq 3\tau$ [96].

Figure 5 shows the ejecta properties as distributions of the normalized ejected mass for the 5- ν (solid lines) and 3- ν (dashed lines) scenarios, as functions of (from left to right) the proton fraction Y_p , the polar angle θ , the temperature T , and the terminal velocity v_∞ . Shown with red lines are the total distributions, while green and blue lines refer respectively to $\bar{t} \leq 4.0$ ms (≤ 6.5 ms) and $\bar{t} \geq 4.0$ ms (≥ 6.5 ms) for SFHo (DD2) EOS to distinguish the properties around the merger from those in the post-merger. Overall, we find that differences emerge between the 5- ν and 3- ν scenarios, with muonic mergers yielding around twice more neutron-rich ejecta in the range $Y_p \sim 0.05$ – 0.1 , suppressing proton-rich ejecta ($Y_p \lesssim 0.3$), and producing ejecta that have lower T , higher s and are less concentrated at high latitude ($\theta < 45^\circ$). These behaviors depend only weakly on the EOS, although the stiffer DD2 EOS tends to weaken the impact of muonic interactions, as already discussed in the main text for the production of lanthanides (see also SM).

SUPPLEMENTAL MATERIAL

Here we provide supplementary information about the results of the simulations are either complement that provided in the main text for the SFHo EOS, or contrast the results when considering binaries evolved with the DD2 EOS [54].

We start by comparing and contrasting the EOS influence on (de-)muonization using Fig. 1 here, which reports equatorial distributions of the temperature T (left portions) and muon fraction Y_μ (right portions) during the inspiral (left column), merger (middle column), and post-merger (right column) phases of a $5-\nu$ scenario with the SFHo (top row) and the DD2 (bottom row) EOS. For each panel, the left portion reports. During the inspiral, we measure values $Y_\mu \approx 0.022$ (≈ 0.032) at the stellar centers for the SFHo (DD2) EOSs, which are essentially determined by the neutrinoless β -equilibrium and negligible muonic interactions. Note that the higher central muon fraction ($Y_\mu \approx 0.032$) for the DD2 EOS in neutrinoless β -equilibrium is essentially determined by the symmetry energy of the EOS [43]. However, rapid muonization at merger drives Y_μ to values $\simeq 0.036 - 0.048$ ($\simeq 0.035-0.040$). Subsequently, a gradual de-muonization takes place during post-merger, which is attributed to the slowly cooling remnant and disk over the dynamical timescale. In this phase, muons are present mostly in the hot shell clearly visible in the temperature distribution.

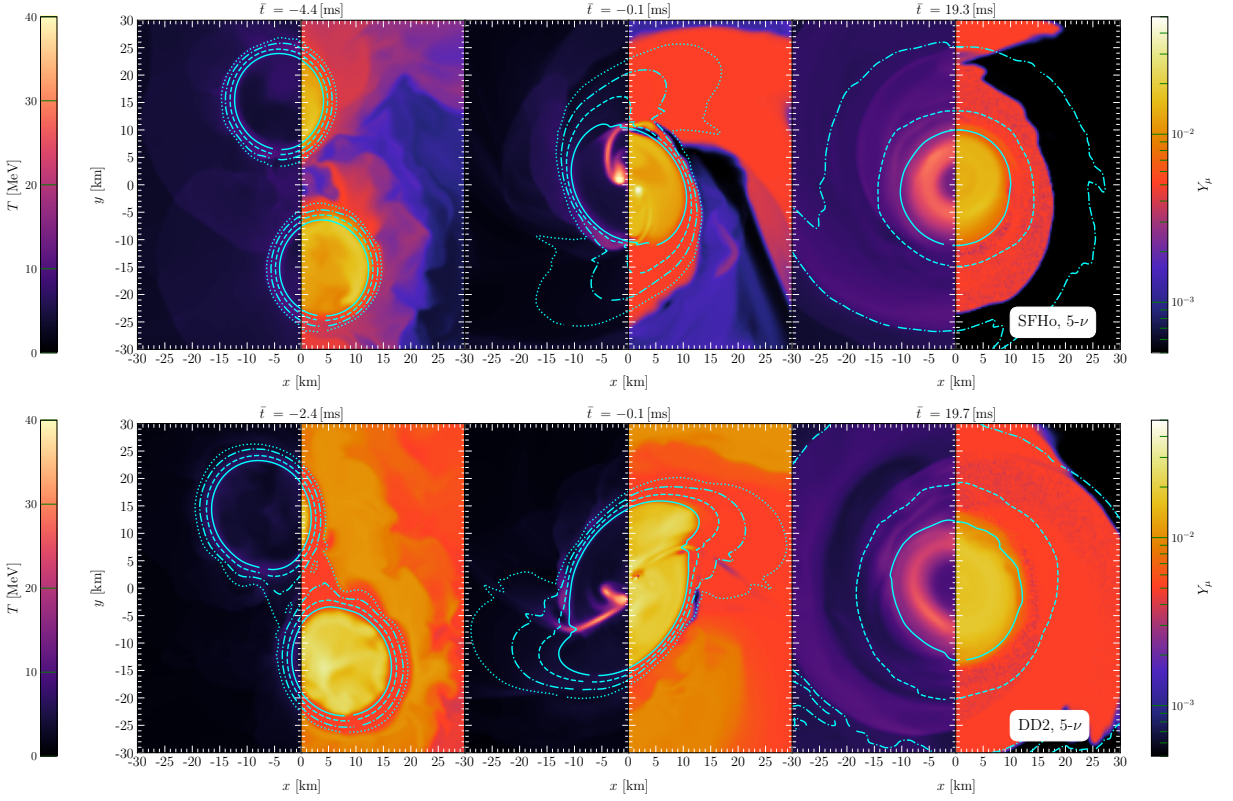


FIG. 1. *Columns, left to right:* Equatorial snapshots of the $5-\nu$ scenarios for the SFHo (*upper*) and DD2 (*bottom*) at the inspiral, merger, and post-merger phases, where *left (right)* of each panel is associated with T (Y_μ). The dotted, dash-dotted, dashed, and solid lines show rest-mass density contours at 10^{11} , 10^{12} , 10^{13} , and 10^{14} g cm^{-3} , respectively, highlighting the dependence of muonization on high density and temperature.

To further quantify these observations, we report in Fig. 2 here the evolution of the mass-averaged potentials in the (x, y) -plane, $\langle \mu_\Delta \rangle_{xy}$, which describe the $npe\nu$ and $np\mu\nu$ equilibria in both $5-\nu$ and $3-\nu$ scenarios for the SFHo (top panel) and DD2 EOS (bottom panel). Despite residual contributions from regions with $\rho < 10^{14}$ g cm^{-3} , we find that $\langle \mu_\Delta \rangle_{xy}$ converges to a nearly constant value close to zero for both equilibria. This occurs on a timescale of $\bar{t} \approx 7-9$ ms ($\bar{t} \approx 11-17$ ms) for the SFHo (DD2) EOS, which is indicated by the shaded regions. We explain the longer timescale for DD2 to achieve equilibria in terms of a lower rest-mass density and temperature of the matter in the matter, which results in a reduction of weak interaction rates. More importantly, both $5-\nu$ and $3-\nu$ scenarios achieve $npe\nu$ equilibrium on similar timescales, affirming the robustness of these

equilibrations across scenarios and EOSs.

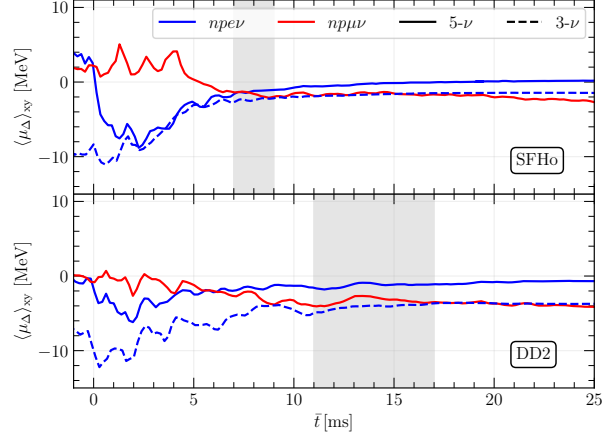


FIG. 2. Evolutions of the mass-averaged out-of-weak-equilibrium potentials $\langle \mu_{\Delta} \rangle_{xy}$ for the 3- ν (dashed lines) and 5- ν scenarios (solid lines) when employing the SFHo EOS (top panel) or the DD2 EOS (bottom panel). Both $npe\nu$ and $n\bar{p}\mu\nu$ equilibria with asymptotic values $\mu_{\Delta}^{npe\nu} \approx \mu_{\Delta}^{n\bar{p}\mu\nu} \approx 0$ in the grey-shaded regions that are reported also in Fig. 1 in the main text and Fig. 3 here.

Interestingly, the timescales over which $\langle \mu_{\Delta}^{n\bar{p}\mu\nu} \rangle_{xy} \approx 0$ correlate with the decrease in the muonic neutrino luminosities $\mathcal{L}_{\nu_{\mu}}$ and $\mathcal{L}_{\bar{\nu}_{\mu}}$ shown in the top part of Fig. 1 in the main text for the SFHo EOS and in the similar Fig. 3 shown here for the DD2 EOS. These reduced luminosities follow from the fact that muonic β -processes, primarily occurring in high-density regions, reach equilibrium from both sides of reaction processes for (anti)neutrino absorption and (anti)lepton capture [see interactions (c) and (d) in Table 1 of EM]. Overall, the stiffer DD2 EOS results in lower rest-mass densities and weaker heating at merger, reducing $\mu^{-}\mu^{+}$ pair production, as muonic contributions in the EOS have less effect on the specific internal energy and pressure for matter at lower density and lower temperature.

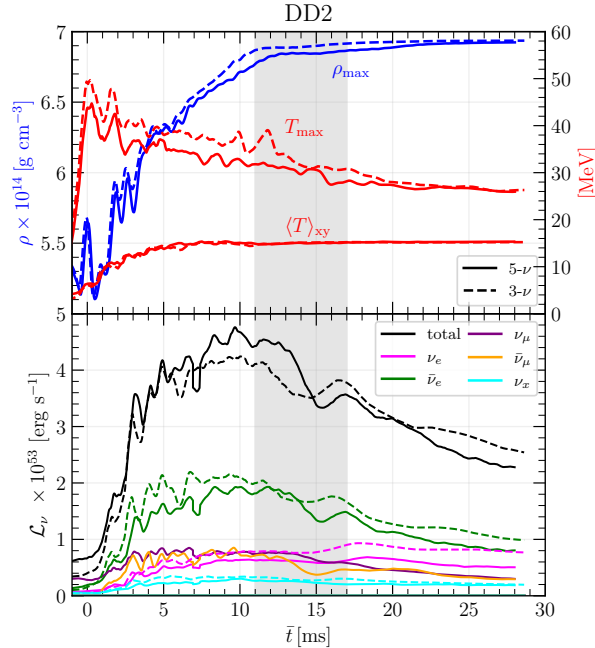


FIG. 3. The same figure as Fig. 1 in the main text, but for the DD2 EOS.

The impact of a weaker muonization as a result of the stiffer DD2 EOS can be appreciated also from the bottom panel of Fig. 3 here, which shows that, unlike the SFHo 5- ν scenario, $\mathcal{L}_{\nu_{\mu}}$ for the DD2 5- ν scenario exceeds $\mathcal{L}_{\bar{\nu}_{\mu}}$ slightly, and the luminosities of muon flavor (anti)neutrinos are reduced, amounting to only about 50% of $\mathcal{L}_{\bar{\nu}_{e}}$ at the early stage. On the other

hand, $\mathcal{L}_{\bar{\nu}_e} \approx \mathcal{L}_{\nu_\mu} \approx \mathcal{L}_{\bar{\nu}_\mu}$ in the first $\bar{t} = 7$ ms for the SFHo EOS. Therefore, weaker muonic interactions result in smaller differences in the total luminosity between the 3- ν and 5- ν scenarios, with the latter consistently showing higher luminosity until $\bar{t} \approx 15$ ms. Two additional remarks are worth making. First, the difference in $\mu_{\bar{\nu}_e}$ at $\rho > 10^{14}$ g cm $^{-3}$ between these scenarios is also smaller for the DD2 EOS. Second, the reduction in energy consumed by muonic processes leaves more energy for e^+ capture, thereby mitigating the reduction in $\mathcal{L}_{\bar{\nu}_e}$. Consequently, the reduction of protonization by muonic processes is less pronounced.

Figure 4 here, which twins Fig. 3 in the main text but for the DD2 EOS, shows a behavior for the proton fraction that is qualitatively very similar to that already discussed for the SFHo EOS, but showing smaller differences between the 5- ν and 3- ν scenarios as a result of the milder densities and temperatures. Overall, this confirms the robustness and self-consistency of our modelling of muonic interactions both at the level of the EOS and of the neutrino transport.

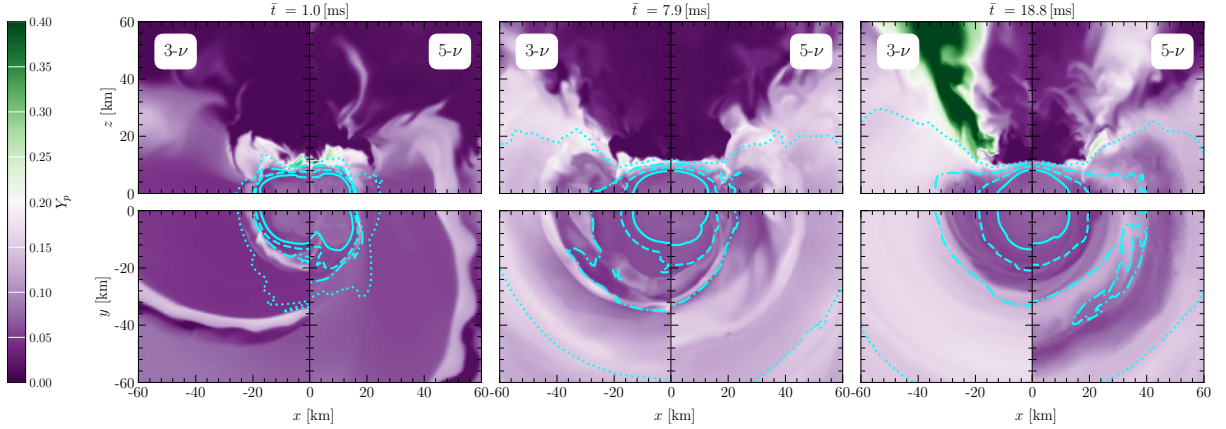


FIG. 4. The same figure as Fig. 3 in the main text, but for the DD2 EOS. Note that the five neutrino-species scenario shows a smaller decrease in Y_p when compared to SFHo EOS.

The amount of the ejected mass and its composition is largely a function of the differences in the merger and post-merger phenomenology and therefore on the on the EOS. To complement Fig. 5 in the End Matter, Fig. 5 here shows the time evolution of the accumulated ejecta mass for both the 3- ν and 5- ν simulations using the SFHo and DD2 EOSs. The total ejecta masses for the 5- ν (3- ν) scenario is respectively $1.63 \times 10^{-3} M_\odot$ ($3.64 \times 10^{-3} M_\odot$) for the SFHo EOS and $4.8 \times 10^{-4} M_\odot$ ($8.6 \times 10^{-4} M_\odot$) for the DD2 EOS. A smaller amount of ejected mass for stiff EOSs is not surprising, especially when considering neutrino emission, and has been reported in a number of studies [1]. Quite generically, this reduction arises from weaker shocks during the merger and post-merger, but also from remnants that are cooler (see also [69]). In our simulations, this corresponds to temperatures that in the DD2 case are $\simeq 5$ MeV ($\simeq 1$ MeV) lower than for the softer SFHo EOS in the 5- ν (3- ν) scenario.

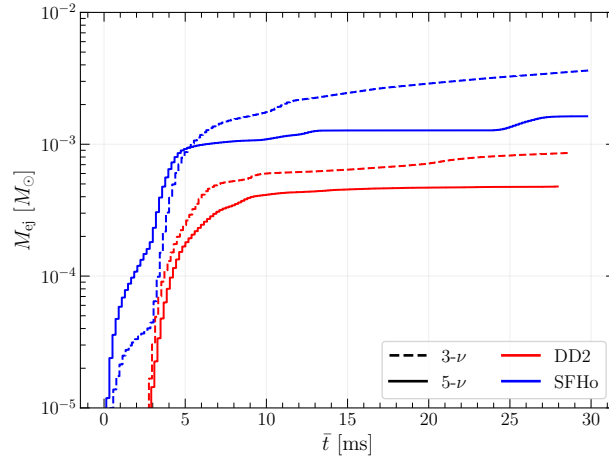


FIG. 5. Comparison of the accumulated ejecta mass for 5- ν and 3- ν scenarios and for the DD2 and SFHo EOSs. Here we find 5- ν consistently results in lower post-merger ejecta for both EOSs.

What is however novel and important is the fact that, for both EOSs, the $5-\nu$ simulations yield significantly less ejected matter than the $3-\nu$ scenarios. Also different is the amount of matter ejected around the merger from the matter ejected on longer timescales. In particular, in the case of the simulations with five neutrino species and the soft EOS, a larger amount of matter is ejected at the merger when compared with the scenario employing three neutrino species. This difference is not present in case of the stiffer DD2 EOS. More precisely, in the DD2 simulations, the post-merger ejecta (i.e., reaching the detector in the first ~ 5 ms) account for only 16% (25%) of the total ejecta mass for $5-\nu$ ($3-\nu$) scenario, while with the SFHo EOS, they contribute 78% (320%) for $5-\nu$ ($3-\nu$) scenario. This difference is driven mostly by the muonic interactions that lead to a more abundant neutrino emission in the early post-merger phase and that lead to a cooler remnant and disk.

Finally, we discuss the chemical composition of the ejected matter after it has undergone r -process nucleosynthesis. This is shown in Fig. 6 here, that twins Fig. 4 in the main text and that is relative to the SFHo EOS. We have already mentioned in the main text that in the latter case, the inclusion of five neutrino species leads to larger abundances of elements with mass number $139 < A < 176$ (blue-shaded region), and to almost an order of magnitude larger yields for elements with $190 < A < 215$ (orange-shaded region). However, in the case of the stiffer DD2 EOS, these differences are much smaller and, indeed, we measure lanthanide yields that are reduced by $\sim 10\%$ when considering five neutrino species.

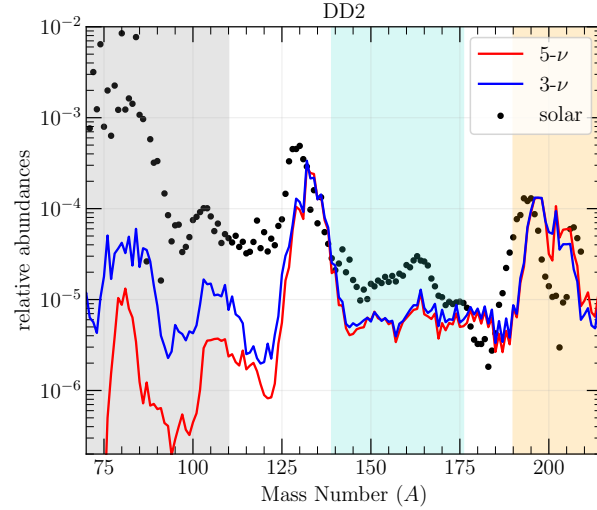


FIG. 6. The same figure as Fig. 4 in the main text but for the DD2 EOS.

This different behavior can be explained in a number of ways. First, via the lower temperatures and densities producing weaker shocks for the DD2 EOS (see also [69]), which eject significantly less matter. Second, via the smaller impact of muonization, that intrinsically requires higher temperatures and densities, hence is more prominent in softer EOSs. Finally, via the smaller reduction of proton fraction in the post-merger (see Fig. 4 here) that naturally impacts nucleosynthesis. As a concluding remark we note that the lack of a “lanthanide boost” in the stiffer DD2 EOS may also be the result of the limited timescale over which our simulations have been carried out. Indeed, it is possible that muonic interactions may require longer timescales to increase lanthanide production in stiff EOSs. We plan to explore this conjecture in future works covering longer post-merger timescales.